Author Manuscript

Author Manuscript

Author Manuscript

Author Manuscript

HHS Public Access

Author manuscript

Nat Mater. Author manuscript; available in PMC 2019 December 01.

Published in final edited form as:

Nat Mater. 2018 December ; 17(12): 1154–1163. doi:10.1038/s41563-018-0182-6.

Injectable tissue integrating networks from recombinant polypeptides with tunable order

Stefan Roberts[1], **Tyler S. Harmon**[2,4], **Jeffery Schaal**[1], **Vincent Miao**[1], **Kan (Jonathan) Li**[3], **Andrew Hunt**[1], **Yi Wen**[1], **Terrence G. Oas**[3], **Joel H. Collier**[1], **Rohit V. Pappu**[4], and **Ashutosh Chilkoti**[1,*]

[1]Department of Biomedical Engineering, Duke University, Durham, North Carolina, 27708, USA

[2]Department of Physics, Washington University in St. Louis, St. Louis, Missouri 63130, USA

[3]Department of Biochemistry, Duke University, Durham, North Carolina, 27708, USA

[4]Department of Biomedical Engineering and Center for Biological Systems Engineering, Washington University in St. Louis, St. Louis, Missouri 63130, USA

Abstract

Emergent properties of natural biomaterials result from the collective effects of nanoscale interactions among ordered and disordered domains. Through recombinant sequence design, we have created a set of partially ordered polypeptides (POPs) to study emergent hierarchical structures by precisely encoding nanoscale order-disorder interactions. These materials, which combine the stimuli-responsiveness of disordered elastin-like polypeptides and the structural stability of polyalanine helices, are thermally responsive with tunable thermal hysteresis and the ability to reversibly form porous, viscoelastic networks above threshold temperatures. Through coarse-grain simulations, we show that hysteresis arises from physical crosslinking due to mesoscale phase separation of ordered and disordered domains. Upon injection of POPs designed to transition at body temperature, they form stable, porous scaffolds that rapidly integrate into surrounding tissue with minimal inflammation and a high degree of vascularization. Sequence level modulation of structural order and disorder is an untapped principle for the design of functional protein-based biomaterials.

---

[*]**Corresponding Author**: Ashutosh Chilkoti: chilkoti@duke.edu.

Author Contributions

S.R. designed and performed experiments, analyzed data, and prepared the manuscript. T.S.H. designed and performed the coarse-grained simulations and co-developed the phenomenological model for hysteresis. J.S. designed, performed, and analyzed *in vivo* work. K.L. designed and performed structural characterization with NMR and CD. A.H. and V.M. constructed POPs and characterized their phase behavior. V.M. also performed rheological experiments. Y.W. designed and aided in vivo experiments. T.O. provided guidance and analyzed data for POP structural characterization. J.C. provided guidance for in vivo experiments. R.V.P. provided guidance, developed the conceptual framework for hysteresis, analyzed results from the coarse-grained simulations, and contributed to preparing the manuscript. A.C. provided guidance, designed experiments, and prepared the manuscript. All authors participated in discussion of the data and in editing and revising the manuscript.

Competing Financial Interests

The authors declare no competing financial interests for this work.

Data Availability

The authors declare that all data supporting the findings of this study are available within the manuscript and its supplementary files and are available from the authors on reasonable request.

Author Manuscript Author Manuscript Author Manuscript Author Manuscript

Many useful properties of soft polymeric materials emerge from the collective interactions amongst ordered and disordered domains. This phenomenon is also one of the hallmarks of naturally occurring and designed protein-based materials. Silk fibers, for example, owe their extraordinary combination of elasticity and strength to the interactions among periodically repeated beta sheets and unstructured domains encoded by the primary sequence[1]. Similarly, tropoelastin—the soluble precursor of elastin—consists of repeats of unstructured hydrophobic regions interspersed by alanine-rich alpha helices[2]. Recent insights into intrinsically disordered proteins (IDPs) highlight the importance of synergy among disordered regions and ordered domains as determinants of function and emergent phase behavior in multivalent proteins[3,4].

To answer how the combination of sequence-encoded order and disorder leads to the emergence of novel macroscopic material properties, nanoscale modules have to be synthesized with molecular precision. The recombinant synthesis of peptide polymers makes it possible to design building blocks with precise, genetic control, enabling ordered and disordered components to be mixed and matched at will within a single polypeptide chain[5]. Here, we report the successful design of modular polypeptides wherein we periodically insert an ordered domain into a disordered polypeptide scaffold. This allows us to uncover the impact of single chain interactions amongst ordered domains and disordered regions on macroscopic material properties.

Polymer Library Design

We chose elastin-like polypeptides (ELPs) as our disordered component. These polymers constitute a family of repetitive polypeptides that are based on a consensus (VPGXG) pentapeptide repeat derived from the disordered regions of tropoelastin. ELPs exhibit tunable lower critical solution temperature (LCST) phase behavior, and they serve as models of elastomeric disorder[6,7]. The sequence-encoded intrinsic disorder of ELPs is thought to be responsible for the observed LCST behavior[6,8]. ELPs are biocompatible polymers with numerous applications in protein purification, drug delivery, and tissue engineering[9].

Our design criterion for the incorporation of ordered domains into disordered scaffolds required that the folded state be autonomously achievable within monomeric forms of the ordered domains. This criterion ruled out the choice of domains that fold upon oligomerization or fully folded protein domains that could disrupt the desired modularity. We hence settled on a design based on the exon organization of tropoelastin. Polyalanine helices are an important structural element of tropoelastin, where they combine with disordered domains to produce the elasticity and resilience that make elastin an important component of the extracellular matrix[10,11]. Because polyalanine sequences are also known to have high intrinsic alpha-helicity in aqueous systems[12,13], they also satisfied our requirements for autonomous folding. We hence hypothesized that recombinant polymers composed of minimalized polyalanine domains doped into an ELP scaffold, mimicking the composition and blocky architecture of tropoelastin[2], would produce biomaterials with unique, tunable properties.

Author Manuscript Author Manuscript Author Manuscript Author Manuscript

Four polyalanine helices (H1–5) with different charge distributions were incorporated into three ELPs (E1–3) of varying side chain hydrophobicities at either 6.25%, 12.5%, 25%, or 50% of the total amino acid number (Figure 1a). Polyalanine domain compositions were chosen to maximize helicity while controlling hydrophilicity through charge-charge interactions. ELP compositions were chosen to span a range of LCSTs suitable for *in vivo* injection[7]. The naming convention for our partially ordered polymers (POPs) specifies the ELP (E*X*), the helix (H *Y*), and the percent helicity (*Z*%): E*X*-H *Y*-*Z*%. The molecular weights and purities for all polymers are detailed in Supplementary Table 1 and Supplementary Figure 1, respectively.

Structural characterization

We used ultraviolet circular dichroism (UV-CD) to determine POP secondary structure. All POPs show the negative ellipticity peaks at 222 nm and 208 nm (Figure 1b-d and Supplementary Figure 2) characteristic of α-helices. Peak magnitudes are largely independent of polyalanine and ELP composition but are highly dependent on total polyalanine percentage. The helices are thermally stable with the lowest melting temperatures greater than 65 ºC (Supplementary Figure 2). However, because quantitative analysis of UV-CD (Supplementary Table 2) for disordered proteins is known to be inaccurate[14,15] and polyalanines can sometimes form beta-rich fibrils[16] we also used 2D-solution NMR to confirm and to quantify POP helicity. Combinations of triple resonance NMR spectra were used for residue assignment, and helicity was determined based on the backbone carbonyl carbon chemical shifts of identified alanine peaks in the H(N)CO spectra (Figure 1f-g and Supplementary Figure 3). Analysis of NMR data showed that 90% of the residues within each polyalanine domain are in a helical conformation at 20˚C, a result that is supported by predictions from helix-coil theory (Figure 1e)[17,18].

Sharp Phase Behavior and Tunable Hysteresis

ELPs exhibit reversible LCST behavior, cycling between an optically clear solution phase and a turbid phase. We measured the thermal phase transition of our POPs by monitoring their optical turbidity as a function of temperature. Remarkably, all proteins demonstrate very sharp phase transitions (1–2°C) range, even when composed of 50% α-helix (Figure 2 and Supplementary Figure 4). These transition temperatures (T_t) vary depending on the specific ELP and helix composition due to differences in their hydrophilicity and charge, but all POPs exhibit the sharp phase behavior characteristic of fully disordered ELPs.

When turbid POP solutions are cooled, they form clear solutions; however, one aspect of their behavior was of particular interest— the marked downshift in the inferred T_t during cooling, designated here as T_t-cooling, when compared to the T_t along the heating leg, designated here as T_t-heating. This thermal hysteresis, defined as the difference between T_t-heating and T_t-cooling, or ΔT_t, is not observed in ELPs although it has been advantageous in other recombinant polymers for the development of hyper-stable micro-particles and for stabilizing protein scaffolds[19–21]. However, the inability to tune the temperature range over which hysteresis occurs in these systems has severely impeded their application.

Author Manuscript Author Manuscript Author Manuscript Author Manuscript

In contrast, the thermal hysteresis in POPs can be precisely controlled as it is directly correlated with polymer helicity (Figure 2a) and is inversely correlated with the amount of charge on the helix side chains (Figure 2b-d and Supplementary Figure 4). Importantly, once fully solvated, POPs return to their original state and can be cyclically heated and cooled with no permanent alterations in their solubility (Figure 2f). By incorporating helices that engender sufficient charge repulsion amongst helices, such as H3, hysteresis can be eliminated altogether. Hysteresis is independent of both heating and cooling rates, and polymers heated and then cooled to their hysteretic range remain aggregated after 24 h (Supplementary Figure 5). Subsequent cooling below the T_t-cooling after 24 h causes rapid dissolution.

For POPs, the T_t-heating scales logarithmically with polymer concentration, in accordance with ELP behavior[7]. However, T_t-cooling is independent of concentration (Figure 2c-e). Altering the ELP composition adjusts the T_t-heating, but it does not change the T_t-cooling (Figure 2e). These observations indicate that the composition and chain length of the ELP segment control T_t-heating, whereas the helix composition is the primary determinant for T_t-cooling. Tuning these two independent parameters —composition of the ELP segment and the fraction and composition (alanine versus charge content) of helix-spanning residues in the POP— provides a sequence-encoded dial to tune the temperature for the onset and the range of thermal hysteresis.

These attributes are likely useful for applications that require hysteresis to encode memory effects. As proof-of-concept for the functional utility of thermal hysteresis, we designed diblock copolymers with a hydrophobic POP and a hydrophilic ELP segment, creating self-assembling nanoparticles with "shape-memory" (Supplementary Figure 6). The POP-ELP diblock self-assembles upon heating above the T_t-heating of the POP core block, but does not disassemble until below its T_t-cooling. These nanoparticles are hence stable within a hysteretic range, once formed. The rational design of protein nanoparticles with controllable kinetic stability, defined in terms of the value of ΔT_t, may offer an intermediate option for drug delivery between physically crosslinked micelles that disassemble in blood upon dilution below their critical micelle concentration, and chemically crosslinked micelles, which must rely on bond cleavage or protease degradation for drug release.

A molecular model for the mechanism of hysteresis

Thermal hysteresis is commonly attributed to changes in secondary structure[21,22]. Because polyalanine can adopt random coil, polyproline II, alpha-helical, and beta-sheet structures[23], we first analyzed POPs to determine if hysteresis derives from changes in secondary structure upon aggregation. UV-CD spectra of a hydrophilic POP (E1-H3–25%) indicate that, in the absence of self-associations, the polymers retain a high degree of helicity up to at least 65 ˚C (Supplementary Figure 2). Phase separating POPs show distortions in the UV-CD spectra consistent (Supplementary Figure 7) with those observed for helical bundles of tropoelastin[24,25]. These spectral shifts suggest the presence of bundled helices within the POP assemblies. This observation is consistent with the coacervation of tropoelastin, in which polyalanine domains retain their structural integrity during coacervation to stabilize side-chain interactions for crosslinking[26,27].

Author Manuscript Author Manuscript Author Manuscript Author Manuscript

Given the intrinsic tendency of polyalanine to form helical bundles[12,16] and the persistence of helices within POP aggregates, we propose helical bundling as a significant contributor to hysteresis. To test this proposal, we performed proof-of-concept assessments using coarse grain molecular dynamics simulations. We used a phenomenological model separating the protein domains into two categories of pentapeptide "beads": polyalanine (AAAAA) and ELP (VPGVG). Because polyalanine is observed to self-associate, the interaction energies between polyalanine beads (E_{AA}) are chosen to be favorable and independent of temperature; ELP interaction energies (E_{EE}) change with temperature, increasing in strength above the T_t-heating. ELP-polyalanine interactions (E_{EA}) are always unfavorable.

We simulated a hysteretic cycle for 50 polymers of 25% helicity (E1-H1–25%) in a 25 nm radius spherical box (Supplementary Materials). The results (Figure 3) suggest that POPs move through four stages during a thermal cycle. (1) Below their T_t-heating, POPs are isolated oligomers with local helical clusters solvated by ELPs. (2) Above the T_t-heating, localized clusters dock due to the increased favorability of ELP hydrophobic interactions. (3) Given sufficient time, alanine domains exchange with neighboring clusters such that single POPs span multiple clusters, entangling them into a network. Swapping helices between clusters is feasible given their high density in the docked state and is thermodynamically favored by entropy of mixing. As the temperature increases further and the ELP repulsive term further decreases, a second reversible transition becomes favored where docked spherical clusters convert into denser, less dynamic linear aggregates— a transition similar to a sphere-to-rod transition for micelles. Above T_t-heating, the ELP domains become less soluble, requiring less surface area. Changes in the ratio of surface area to volume can lead to thermodynamic preference for rods over spheres[28]. (4) Once cooled below the T_t-heating, the entanglement of aggregates prevents the dissolution of ELP domains, producing entangled oligomers. Unlike the fast and irreversible transition from docked aggregates to entangled aggregates (2–3), transitions between entangled oligomers and isolated oligomers are slow. A sufficient drop in ELP interaction energy (below T_t-cooling) leads to solvation of the POPs, diluting the clusters and returning them to their original state.

Formation of solid-like, fractal networks

The macroscopic properties of POP aggregates also indicate an aggregation mechanism distinct from the liquid coacervation of disordered ELPs. Rather than a turbid suspension, POPs transition into mechanically stable, opaque aggregates. These aggregates undergo syneresis at high temperatures, cracking and shrinking at temperatures considerably above the T_t-heating (Figure 4a). Syneresis suggests percolated crosslinking interactions among polymers[29], likely due to network formation from the helical clustering predicted by our simulations.

We performed oscillatory rheology on POPs to characterize key mechanical network properties and compare them to ELP controls (Supplementary Fig 8–9). Frequency sweeps in the linear viscoelastic region of ELPs above their T_t show their loss modulus (G'') (23Pa, 1 Hz, 10 wt%) to be greater than the storage modulus (G') (8.0 Pa, 1 Hz, 10 wt%) and both to be proportional to frequency. This behavior is consistent with liquid-like coacervates[30]. In contrast, at equivalent concentrations, POPs exhibit a G' (12.2 kPa, 1 Hz) that is much

Author Manuscript Author Manuscript Author Manuscript Author Manuscript

greater than G" (0.36 kPa, 1Hz), close to three orders of magnitude higher than the G' of equivalent ELPs, and independent of frequency. This behavior is typical of more solid-like materials[30]. POPs also display high viscosity with plastic, shear-thinning flow, while ELPs behave as Newtonian fluids. The shear-thinning slope for POPs is unusually high (–0.95) for long-chain, polymers indicative of some network rupture, and this observation is consistent with reported values for tropoelastin networks[30].

Importantly, POP mechanical properties can be altered with polymer composition (Supplementary Figure 9). Material stiffness is directly correlated with MW and helical percentage but is unaffected by the composition of the disordered region. Though POP aggregate stability is driven by physical crosslinking, other crosslinking mechanisms may also be used to further modulate mechanical properties. The effect of chemical crosslinking on POPs and the relationship to other chemically crosslinked disordered polymers is detailed in the Supplementary Materials.

The incorporation of helical domains in POPs also affects microscale phase separation (Figure 4b-c). While ELPs form micron-sized coalescing aggregates, forming a colloidal suspension of liquid-like droplets, POPs undergo arrested phase separation into porous networks. POPs with only a single helix form coacervates similar to fully disordered ELPs (Supplementary Figure 11), indicating that physical crosslinks between helical domains from separate POP chains are necessary for network formation. These networks have a fractal-like architecture, with E1-H5–12.5% and E1-H5–25% POP networks having fractal dimensions between 1.6 and 1.9, dependent on POP concentration (Supplementary Figure 10). This fractal dimension is comparable to that observed for native elastin networks[31]. We highlight the fractal-nature of POP networks as an intriguing observation because fractals are ubiquitous in nature yet difficult to artificially recreate. Beyond biomimicry, we make no claims for their utility at this time.

We next used structured illumination microscopy (SIM), a super-resolution microscopy technique[32], to further characterize POP networks. SIM reveals the presence of interconnected mesoscale polymer globules no larger than 200 nm (Figure 4d). This architecture is consistent across multiple polymer compositions (Supplementary Figure 12) and suggests a two-stage aggregation process. POPs initially nucleate like their disordered ELP counterparts at their T_t-heating, driven by the disordered domains. Rather than coalesce, as the solution temperature is raised beyond T_t-heating the mesoscopic nuclei rapidly link, forming fractal networks. Our coarse-grained simulations also predict a two-stage process on the nanoscale (aggregate docking and entanglement), and we propose that similar entanglements must also occur on the meso and micro-scales. This type of aggregation is mirrored in tropoelastin, which undergoes a multistage process[27] that includes an initial hydrophobic coacervation into spherical droplets and subsequent maturation into networks or fibers due to interactions between crosslinking domains[27,33]. Note that the effects of physical crosslinking due to polymer entanglements are notably distinct from those of chemical crosslinking (Supplementary Figure 13 and Supplementary Discussion).

We also measured the internal mobility of POP networks by monitoring their fluorescence recovery after photobleaching (FRAP). Minimal recovery was observed after 30 min,

Author Manuscript Author Manuscript Author Manuscript Author Manuscript

suggesting that POP networks are kinetically stable (Figure 5a) due to physical crosslinking from helical bundling within the network. There is slightly more recovery for 12.5% networks compared to 25%, but the unrecovered fraction remains high (86%). We can also control network porosity by modulating polymer concentration. Using three-dimensional reconstructions from confocal microscopy, we evaluated the effects of concentration and polymer composition on total void volume, defined as the non-protein rich phase of the network. Within a range of 50 μM (1.6 mg/ml) to 800 μM (25.6 mg/ml) for E1-H5-(X)%, the void volume can be tuned between 90% (~30–50μm pores) and 60% (~3–5μm pores), with no significant difference in void volume observed between the POPs with 12.5% and 25% helical content over all tested concentrations (Figure 5b-and Supplementary Figure 14). We also measured the void volume for a variety of POP compositions and found that polymer composition—including changes to MW, helical percentage, helix sequence, and ELP sequence—have no measurable impact on void volume (Sup Figure 15). This finding allows us to tune porosity of the POP network independently of other network properties. Having porosity as an independently tunable parameter provides a stepwise means to tailor POP networks to specific applications. Toward this end, we envisage the following protocol to orthogonally tune POP properties: (1) choose porosity with concentration; (2) choose other physical properties (mechanical properties or T_t-cool) with MW, helix sequence and percentage; (3) finally, choose aggregation temperature (T_t-heating) with ELP composition. The ability to tailor POP networks in this manner, and their ability to span 2–3 orders of magnitude in elastic moduli, could be useful, for example, in guiding stem cell differentiation, a mechanism quite sensitive to the mechanical properties of the 3-D culture matrix that also requires control of matrix diffusivity to enable transport of nutrients and signaling factors to cells from the surrounding growth medium[34,35].

Our work departs in significant ways from previous studies on block copolymers of bioactive or mechanically active folded protein domains with disordered sequences such as ELPs[36]. Hydrogels and fibers have been produced with ordered segments such as coiled-coils and leucine-zippers to alter their self-assembly[37,38]; however, these studies have focused on the specific impact of more complicated structural peptides rather than the modular incorporation of ordered versus disordered regions. Likewise, copolymers of disordered domains have produced gels and nanostructures[39–41], but these too lack the interplay of order and disorder as a design principle to encode higher order structure. Recombinant combinations of peptide sequences derived from structural proteins such as collagen and silk with elastin are more closely related to this study[42,43], although neither the precise and tunable control over thermal hysteresis nor the emergence of an interconnected thermally reversible fractal network architecture has been reported in these studies.

Combinations of order and disorder have also been explored in the field of synthetic polymers. Ratios of atactic (disordered) and isotactic (ordered) polymer blocks have long been used to control gelation and even thermal phase transitions[44,45], with threshold percentages of isotactic polymers required for specific material properties. It is striking that the principles that guide the modification of synthetic polymers so readily align to those we have shown herein for bioinspired peptide polymers. Although synthetic polymers and recombinant peptide polymers each have their own advantages, peptide polymers are attractive for biotechnology and biomedical applications because of their native

Author Manuscript Author Manuscript Author Manuscript Author Manuscript

biocompatibility and our ability to design them at absolute molecular levels through recombinant synthesis, making them better suited for tuning material properties via precise —genetically encodable— changes of their amino acid sequence.

In situ network stability and cell penetration

POPs designed to transition below the body temperature (37°C) are advantageous for forming depots *in vivo* since they can be handled and injected as liquids, yet rapidly form viscoelastic materials when injected *in vivo*. Although injectable ELP depots have been used for controlled drug delivery[46], the homogenous liquid nature of non-crosslinked ELP coacervates has limited their applications in tissue engineering[47,48]. Without chemical crosslinking, ELP coacervates lack the mechanical stability and porosity to support cell migration and growth[48]. It has also been shown that porous materials interact more favorably with the immune system, preventing foreign body response and inducing the migration of regenerative immune cells[49,50]. We hypothesized that polypeptides such as POPs, which exhibit thermally triggered hierarchical self-assembly into stable porous networks without the need for chemical crosslinking, may have beneficial in vivo behaviors.

Motivated by this hypothesis, we next assessed the *in vivo* behavior of injected POPs. We injected E1-H5–25%−120 (200 μL at 250 μM, 50 kDa) as sub-cutaneous depots and compared their pharmacokinetic (PK) properties to fully disordered ELPs of the same base sequence. POP depots, labeled with ^{125}I, showed significantly less polymer release (4.8% of initial dose) than their disordered ELP counterparts (8.7%) after 120 hours despite their increased porosity and greater surface area (Figure 6a). Terminal bio-distribution also revealed no critical accumulation in vital organs (Supplementary Figure 16). Upon injection, ELPs diffuse in the sub-cutaneous space until they are not visible externally whereas POPs form large, visibly palpable depots (Figure 6b). Single-photon emission computed tomography (SPECT) confirms that ELP depots are more diffuse than POP depots with higher surface-to-volume ratios and lower polymer densities (Figure 6c and Supplementary Figure 17).

To analyze POP persistence in the sub-cutaneous space and cell recruitment, C57BL/6 mice receiving endotoxin purified (< 1 EU/ml) sub-cutaneous injections of E1-H5–25%−120 (200 μL at 250 μM, 50 kDa) were monitored over 21 days. Injected depots were excised and either fixed for histological evaluation or processed for flow cytometry (Supplementary Methods and Supplementary Fig 18–20). POPs rapidly and robustly integrate into the sub-cutaneous space, creating mechanical connections with surrounding tissue within 24 h (Figure 6e). Importantly, they do not show a significant decrease in size after 21 days (Figure 6d and Supplementary Figures 18,21). Initial cell recruitment is high, with cell density peaking at day 10 (Figure 6f). Recruited cells show that the POP depots undergo a wound healing response with an initial, mild inflammatory phase that resolves over time followed by angiogenesis and proliferation of non-immune cells. Hematopoietic-derived cells (CD45+) steadily increase up to day 10 with neutrophils, inflammatory monocytes, and macrophages peaking on days 1, 3, and 10 respectively (Figure 6g-h). By day 21, all hematopoietic derived cells drop off dramatically and non-hematopoietic cells become the dominant population (Figure 6g-h and Supplementary Figure 21). Curiously, E1-H5–25%

Author Manuscript Author Manuscript Author Manuscript Author Manuscript

−120 injected at 750 μM POP showed minimal differences in recruited cell subtypes from the same POP injected at a concentration of 250 μM (Supplementary Figure 21). As the explants from the 750 μM injections were larger, it is likely that the material was able to spread within the sub-cutaneous space, creating an effectively similar pore size *in vivo*. Histology of POP depots supports the presence of a high cellular density, extensive cellular infiltration from surrounding tissue, and a lack of fibrous capsule formation (Supplementary Figure 22). POPs also show a high degree of vascularization with capillaries and some larger vessels emerging by day 10—with some branching vessels even visible to the unaided eye (Figure 6d,i-j). The vasculature becomes more uniformly distributed throughout the depots by day 21.

Because fully disordered ELPs diffuse too quickly to form explantable depots, we injected equivalent weight percentages of Matrigel for comparison. Given the biochemical differences between POPs and Matrigel, this comparison is only intended to provide a contrast to widely used temperature-sensitive, injectable scaffold. Compared to Matrigel, POPs recruit a greater number of cells, including non-hematopoietic cells, and show dramatically increased mechanical integration and vascularization than Matrigel (Supplementary Figure 23). POPs are likely more useful than Matrigel for applications requiring increased integration of the scaffold into surrounding tissue, whereas Matrigel may be more useful for applications requiring greater initial isolation of the material from surrounding tissue. The angiogenesis of POPs, with minimal inflammation, is promising for their use as injectable materials for regenerative medicine.

Summary and Outlook

Using molecularly engineered polypeptides with precisely encoded ordered and disordered segments, we have developed a simple, modular and tunable material system to evaluate the impact of molecular order and disorder at the primary sequence level on the structure and properties of the resulting material. By encoding helical domains into ELPs, we show that thermally triggered phase separation does not lead to dense, homogeneous coacervates. Instead, POPs drive the hierarchical assembly of porous, physically crosslinked viscoelastic networks architecturally reminiscent of cross-linked elastin. These networks retain the thermal reversibility of fully disordered ELPs; however, and rather strikingly, the aggregation and dissolution temperatures can be independently controlled by specifying the composition and mass fraction of the disordered and ordered domains. POPs assemble into 3D scaffolds *in vivo* that are notably more stable than fully disordered controls. Analysis of explanted POP depots reveals a progression from mild inflammation that resolves with time, to migration of cells within the scaffold, followed by proliferation and vascularization, indicating that POPs promote wound healing and tissue growth. As the field of intrinsically disordered proteins has expanded, knowledge of the biological importance of the synergy between disordered regions and ordered domains has grown; yet limited information exists on functionalizing these interactions for biomedical applications. Our biopolymer platform is an important step towards uncovering design rules that combine order and disorder to develop a new generation of functional protein-based biomaterials.

Author Manuscript

Author Manuscript

Author Manuscript

Author Manuscript

Methods:

Synthesis of polymer genes

All polymers were cloned into a modified pet24 vector using a previously described process known as recursive directional ligation by plasmid reconstruction (PRe-RDL)[5]. Briefly, single stranded oligomers encoding the desired sequences were annealed into cassettes with CC and GG overhangs. The overhangs enabled their concatemerization and ligation (Quick Ligase, NEB, Ipswich, MA) into the pet24 vector. Using this process, we created a library of elastin-like polypeptide and polyalanine cassettes (Supplemental Table 1), which could be strung together through multiple cycles of PRe-RDL to form the final partially ordered polymers. All of the base oligomer cassettes used for polymer construction can be found below. Plasmids were transfected into chemically competent Eb5α (EdgeBio, Gaithersburg, MD) cells for cloning and BL21(DE3) (EdgeBio, Gaithersburg, MD) cells for protein expression.

Expression and purification of POPs

For protein expression, 5 mL starter cultures were grown overnight from −80°C DMSO stocks. Cells were then pelleted, resuspended in 1 mL of terrific broth, and used, along with 1 mL 100 $\mu g.mL^{-1}$ of kanamycin (EMD Millipore, Billerica, MA) to inoculate 1 L of media. Cells were shaken at 200 rpm for 8hrs at 25°C before induction. For induction of protein expression, 1 mL of 1 M isopropyl β-D-1-thiogalactopyranoside (Goldbio, St. Louis, MO) was added to the flask and cultures were placed at 16°C and 200 rpm overnight. Expression at lower temperature was necessary to prevent the formation of truncation products at ELP-polyalanine junctions. Cells were then pelleted and resuspended in 10 mL of 1X PBS for every 1L of culture grown. Pulse sonication on ice, with a total active time of 3 minutes, was used to lyse cells. Cell lysates were treated with 10% PEI (MP Biomedical, Santa Ana, CA) (2 $ml.L^{-1}$ culture) to remove contaminating DNA and centrifuged at 14k rpm for 10min at 4˚C. Polymer was purified from the resulting soluble fraction using a modified version of inverse thermal cycling[51]. The fraction was heated to 65˚C or until phase separation was observed. For more hydrophilic polymers, this often required the addition of 1–2 M NaCl to depress the transition temperature. Once aggregated, the polymer solutions were centrifuged at 14k rpm for 10min at 35˚C, and the resulting pellet was re-suspended in 5–10 ml PBS. The heating and cooling centrifugation cycles were repeated 2–3 more times until a purity of 95% was achieved, as analyzed by sodium dodecyl sulfate polyacrylamide gel electrophoresis (SDS-PAGE). Purified polymers were dialyzed at 4˚C with frequent water changes for 2 days and lyophilized for storage. Final purity and homogeneity were verified by SDS-PAGE, and their MWs were verified by matrix assisted laser desorption ionization mass spectrometry (MALDI-MS); in all cases, the experimentally determined MWs agreed with their theoretical MWs within 2%.

Secondary structure characterization

Circular dichroism experiments were performed using an Aviv Model 202 instrument and 1mm quartz cells (Hellma USA, Plainview, NY). Unless otherwise noted, scans were carried out in PBS (pH=7.4) with a polymer concentration of 10 μM. Polymers were scanned in triplicate from 260 nm to 185 nm in 1 nm steps with a 1 s averaging time. Data points with a

Author Manuscript Author Manuscript Author Manuscript Author Manuscript

dynode voltage above 500 V were ignored in the analysis. All measurements were performed at 20˚C unless otherwise specified. Temperature ramping was done in 5˚C/min increments with a 1 min equilibration at each step. A detailed description of NMR experiments is given in the supplemental materials. In brief, polymers were grown in M9 minimal media with ^{15}N-NH_4Cl and ^{13}C-Glucose (Cambridge Isotopes, Tewksbury, MA) to label the nitrogen and carbons for triple resonance measurements. Helicity was determined based on the alanine peaks of the H(N)CO spectra for E1-H2–25% after resonance assignment.

Temperature-dependent turbidity

The transition temperature (T_t) of each sample was determined by monitoring the optical density at 350nm as a function of temperature on a UV-vis spectrophotometer (Cary 300 Bio; Varian Instruments, Palo Alto, CA) equipped with a multicell thermoelectric temperature controller. The T_t was defined as the point of largest inflection (maximum of the first derivative) for the optical density. Unless otherwise stated, all samples were heated and cooled at 1 °C min^{-1} in PBS at concentrations between 10 and 1000 μm.

Coarse-grained molecular dynamics simulations

See Supplemental Materials.

Rheology

Prior to performing oscillatory shear rheology, samples were prepared in PBS and allowed to equilibrate at 4°C. Measurements were taken on a Kinexus Pro (Malvern, Westborough, MA) using a Peltier heating element and a 10mm parallel plate geometry. Samples were enclosed in a humidified environment to prevent drying during heating, equilibration, and oscillation. Soluble polymer samples were loaded onto the lower portion of the geometry set at 4°C. The upper portion of the geometry was lowered to 0.5mm, and the instrument was subsequently heated to the experimental temperature (37°C unless otherwise specified) and allowed to equilibrate for 30min. To account for volume contraction in ELP and POP gels, samples were run with a normal force control of 0.1N—determined to be the optimal normal force to maintain geometry contact without sample deformation. Uncrosslinked ELP gels were too soft for adequate normal force control, and were instead run with a gap control set to the average gap of their corresponding POP concentration. Each polymer condition was repeated in triplicate. For comparison to chemical crosslinking, an additional ELP ($E1_{80}DK$) was produced which matched the aspartic acid and lysine distribution of E1-H5–25%, with otherwise identical composition to $E1_{80}$. Tetrakis(hydroxymethyl)phosphonium chloride (THPC) was used to crosslink available lysines, and, unless otherwise stated, crosslinker was mixed in a 1:1 molar ratio with polymer lysines (a 4:1 molar ratio with polymer). THPC was added to the polymer solution at 4°C prior heating and equilibration.

Fluorescence imaging and analysis

POPs were fluorescently labeled using Alexa Fluor 488 NHS Ester (Thermo Fisher, Waltham, MA) with a typical reaction efficiency of 20%. Excess dye was removed with dialysis and polymers were lyophilized for storage. For all experiments, the dyed polymers

Author Manuscript

Author Manuscript

Author Manuscript

Author Manuscript

were diluted into an undyed stock such that no more than 5% of POPs in solution were labelled. Confocal images were taken on a Zeiss 710 inverted microscope with temperature controlled incubation. To prevent dehydration, 50μl of sample solution was added to 384 well #1.5 glass bottom plates (Cellvis, Mountain View, CA) for imaging. Solutions were added below the T_t and allowed to transition and equilibrated for 5 minutes on the microscope stage. For FRAP experiments, samples (n=3 for each group) were equilibrated for 30 min to prevent thermal movement of the focusing stage, and fluorescence intensity analysis was done using Zen software (ZEISS Microscopy, Jena, Germany). Samples were bleached for 30s at 90% laser power, and images were collected every 5s for 30min min. Unbleached areas were taken at the same time and fluorescence values were normalized to changes in unbleached areas to account for natural photobleaching with continued laser exposure. For void volume analysis, 20 μm image stacks (n=3 for each concentration) were taken with a pinhole size of 1 Airy unit and vertical slice intervals of 230 nm. Three dimensional reconstructions of the resultant networks and quantification of their void volume were done in IMARIS 8 (Bitplane. Belfast, Ireland). Surface renders were constructed with a minimum object detail of 200nm, the minimal lateral resolution of the confocal microscope, and local background thresholding with the diameter of the largest sphere that fits into the object set a 1μm. A consistent minimum background threshold was used across samples. Network fractal dimensions were determined using the 2D box counting algorithm from the FracLac plugin for ImageJ [52,53]. Structured illumination microscopy images were taken with assistance from Dr. Kai Wang using an in-house microscope constructed at Janelia Farm in the lab of Dr. Eric Betzig. Polymer samples were added to a glass slide at 4°C and allowed to aggregate and equilibrate at 37°C. After equilibration, a cover slip was added, since the SIM was an upright microscope, resulting in some network deformation on the microscale as compared to the confocal images. SIM images were taken with a lateral resolution of ~120nm and an axial resolution of ~300nm. Image stacks were acquired with a z-distance of 150nm, and 15 SIM images were taken for each plane—5 phases and 3 angles. Voxel size for all reconstructed images—done using an in-house algorithm—was 48nm in x,y and 147nm in z. Reconstructed image stacks of 5um were used to created maximum intensity projections for analysis in ImageJ. Additional technical details on the experimental setup have been previously published[54,55].

Pharmacokinetic and SPECT analysis

All constructs were endotoxin purified to < 1 EU/ml and prepared at 500μM in sterilized PBS and reacted with ^{125}Iodine (Perkin Elmer, Boston MA) in Pierce® pre-coated IODOGEN tubes (Fisher Scientific, Hampton, NH)[56]. The product was centrifugally purified through 40K MWCO Zeba Spin Desalting Columns (Thermo Scientific, Rockford, IL) at 2500 rpm for 3 min at 4°C to remove unreacted radioiodine from the conjugate. After labeling, each construct was diluted down to a final biopolymer concentration of 250μM. The resulting activity dose for the POP was 1.18 mCi mL^{-1}, while the ELP dose was 1.37 mCi mL^{-1}.

Female athymic nude mice (7 weeks old) were purchased from Charles River and housed in a centralized animal facility at Duke University. All procedures were approved by the Duke University Institutional Animal Care and Use Committee and were in compliance with the

Author Manuscript Author Manuscript Author Manuscript Author Manuscript

NIH Guide for the Care and Use of Laboratory Animals. 50μL of the POP was prepared in an Eppendorf tube at 63μCi to provide a reference imaging standard. Prior to either the depot injection, blood draw, or single-photon emission computed tomography (SPECT) imaging, each mouse was anesthetized using a 1.6% isoflurane vaporizer feed at an O2 flow rate of 0.6 L min^{-1}. 7For depot injections, each mouse received a soluble 200μL injection of their respective solution at 250μM into the subcutaneous space on the right hind flank. The whole body activity of the mouse was then measured in an AtomLab 400 dose calibrator (Biodex, Shirley, NY). A total of 12 athymic nude mice (n=6 for each group) were used for pharmacokinetic analysis of depot stability and distribution. An initial 10μL blood sample was drawn and pipetted into 1000mg mL^{-1} heparin with subsequent blood draws at time points of 45min, 4h, 8h, 24h, 48h, 72h, 96, and 120h to determine the release profile for the depots. 6 total athylmic nude mice also were imaged using SPECT at time points of 0, 48, and 120 hrs. Mice were then transferred under anesthesia to the bed of the U-SPECT-II/CT for imaging using a 0.350 collimator (MILabs B.V., Utrecht, Netherlands) courtesy of G. Al Johnson in the Duke CIVM. Anesthesia was maintained with a 1.6% isoflurane feed at an O2 flow rate of 0.6 L min^{-1}. SPECT acquisition was conducted over a time frame of 15 minutes in ‘list-mode’ and at a ‘fine’ step-mode. Upon completion, a subsequent CT scan was carried out at a current of 615μA and a voltage of 65kV. Mice were then returned to their cages. Post-imaging SPECT reconstruction was carried out using MILabs proprietary software without decay correction and centered on the ^{125}I photon range of 15–45 keV. All images were reconstructed at a voxel size of 0.2 mm. Reconstructed SPECT images were then registered with their corresponding CT scans to provide spatial alignment for anatomical reference.

Upon completion of the study, all mice were euthanized and dissected. The subcutaneous depots were excised and visually examined for physical differences. In addition, the heart, thyroid, lungs, liver, kidneys, spleen, skin, muscle and pancreas were collected and analyzed using a Wallac 1282 Gamma Counter (Perkin Elmer, Boston, MA) to determine the relative biodistribution of the different constructs. All blood samples and the set of PK standards were similarly analyzed using the gamma counter. The counts per minute detected for each sample were converted to their corresponding activity. Blood samples were then scaled to determine the total amount in circulation according to the formula Total = CPM/.01*BW*72ml/kg[57]. Depot retention was analyzed by measuring the total photon intensity of the depot SPECT image in ImageJ. Measured photon intensity was converted to total depot activity using a calibration factor determined from the imaging standard. This calibration was determined by performing a linear regression of the known activities of the standard over time against the corresponding SPECT intensity measurements. The factor was applied to each depot and the calculated activity compared against the original whole body injected dose at 0h to determine its percent retention.

Cell Recruitment

Female C57BL/6 mice (7 weeks old) were purchased from Charles River and housed in a centralized animal facility at Duke University. All procedures were approved by the Duke University Institutional Animal Care and Use Committee and were in compliance with the NIH Guide for the Care and Use of Laboratory Animals. For analysis of POP persistence

Author Manuscript Author Manuscript Author Manuscript Author Manuscript

and cell recruitment, female C57BL/6 mice (used for their complete immune system over the nude mice used in the previous study for easier depot observation) received soluble injections in the subcutaneous space of the right and left hind flanks. Mice were injected with either 200μl of 250μM E1-H5–25%−120 (19), 200μl of 750μM E1-H5–25%−120 (4), or Matrigel (Standard Formulation, Corning, Tewksbury, MA) (7). POPs were endotoxin purified to < 1 EU/ml and sterile filtered prior to injection. At respective time points, mice were euthanized and dissected. Left hind injections were excised and placed in 10% neutral buffered formalin (Sigma, St. Louis, MO) for histological analysis (n=3 for all groups). Fixed depots were embedded in paraffin, and 5μm slices from the center of each depot were stained with Hematoxylin and Eosin (H&E). H&E stained slides were imaged using an Axio 506 color camera mounted on a Zeiss Axio Imager Widfield microscope. Images at 200x magnification were stitched and exported for analysis. Blood vessels and capillaries were manually counted in ImageJ (n=3). For changes in depot size, images of excised depots were taken at a controlled distance and imported into ImageJ for quantification.

Flow cytometry experimental details, including staining, acquisition, and gating, are given in the supplemental materials. In brief, existed injections were digested, filtered to attain a single cell suspension and stained with markers for hematopoietic cell subtypes (neutrophils, monocytes, macrophages) and non-hematopoietic sub-types (epithelial and endothelial).

Statistics and Reproducibility

All statistical analysis was carried out using Prism 6 (Graphpad Inc, La Jolla, CA). Where box and whisker plots are used, the center line represents the median, the box limits represent the upper and lower quartiles, and the whiskers represent a range of 10–90% of the maximum. Where bar charts are used, individual data points are provided along with standard error (SEM) error bars unless otherwise specified. When comparing individual groups, two-tailed t-tests were used to determine statistical significance. ANOVA was used to evaluate significance among three or more groups and the Tukey-Kramer or Dunnett's methods were used as a post hoc tests where indicated in the text for comparisons between groups. Experimental group sizes are given within the descriptions of each experiment.

All CD, optical density, microscopy (confocal and SIM), rheology, and light scattering experiments were repeated at least three times, with similar results. NMR spectral analysis was repeated twice, with similar results. Polymers were purified several times from independent stocks to ensure observed behavior was not batch dependent. For animal experiments, repetition was conducted where possible without unnecessary use of animals. Histological evaluations were repeated at least three times, with similar results, and where representative images are used in the main text (e.g., SPECT and explanted depots) a range of additional images are provided in the supplemental information.

Supplementary Material

Refer to Web version on PubMed Central for supplementary material.

Author Manuscript Author Manuscript Author Manuscript Author Manuscript

Acknowledgments

We thank Dr. Kai Wang for his invaluable help with SIM imaging and Dr. Eric Betzig for use of his facilities at Janelia Farms for SIM. This work was funded by the NIH through grants GM061232 to A.C. and R01NS056114 to R.V.P., by the NSF through grants from the Research Triangle MRSEC (DMR-11–21107), NSF DMFREF (DMR-1729671) to A.C., MCB-1614766 to R.V.P., and through the Graduate Research Fellowship Program under Grant No. 1106401 to S.R.

References

1. Keten S, Xu Z, Ihle B & Buehler MJ Nanoconfinement controls stiffness, strength and mechanical toughness of beta-sheet crystals in silk. Nat Mater 9, 359–367, doi:10.1038/nmat2704 (2010). [PubMed: 20228820]
2. Tamburro AM, Bochicchio B & Pepe A Dissection of human tropoelastin: exon-by-exon chemical synthesis and related conformational studies. Biochemistry 42, 13347–13362, doi:10.1021/bi034837t (2003). [PubMed: 14609345]
3. van der Lee R et al. Classification of intrinsically disordered regions and proteins. Chem Rev 114, 6589–6631, doi:10.1021/cr400525m (2014). [PubMed: 24773235]
4. Harmon TS, Holehouse AS, Rosen MK & Pappu RV Intrinsically disordered linkers determine the interplay between phase separation and gelation in multivalent proteins. eLife 6, e30294 (2017). [PubMed: 29091028]
5. McDaniel JR, Mackay JA, Quiroz FG & Chilkoti A Recursive directional ligation by plasmid reconstruction allows rapid and seamless cloning of oligomeric genes. Biomacromolecules 11, 944–952, doi:10.1021/bm901387t (2010). [PubMed: 20184309]
6. Roberts S, Dzuricky M & Chilkoti A Elastin-like polypeptides as models of intrinsically disordered proteins. FEBS Lett 589, 2477–2486, doi:10.1016/j.febslet.2015.08.029 (2015). [PubMed: 26325592]
7. McDaniel JR, Radford DC & Chilkoti A A unified model for de novo design of elastin-like polypeptides with tunable inverse transition temperatures. Biomacromolecules 14, 2866–2872, doi:10.1021/bm4007166 (2013). [PubMed: 23808597]
8. Pometun MS, Chekmenev EY & Wittebort RJ Quantitative observation of backbone disorder in native elastin. J Biol Chem 279, 7982–7987, doi:10.1074/jbc.M310948200 (2004). [PubMed: 14625282]
9. MacEwan SR & Chilkoti A Elastin-like polypeptides: biomedical applications of tunable biopolymers. Biopolymers 94, 60–77, doi:10.1002/bip.21327 (2010). [PubMed: 20091871]
10. Gosline J et al. Elastic proteins: biological roles and mechanical properties. Philos Trans R Soc Lond B Biol Sci 357, 121–132, doi:10.1098/rstb.2001.1022 (2002). [PubMed: 11911769]
11. Lillie MA & Gosline JM The viscoelastic basis for the tensile strength of elastin. Int J Biol Macromol 30, 119–127 (2002). [PubMed: 11911903]
12. Miller JS, Kennedy RJ & Kemp DS Solubilized, Spaced Polyalanines: A Context-Free System for Determining Amino Acid α-Helix Propensities. Journal of the American Chemical Society 124, 945–962, doi:10.1021/ja011726d (2002). [PubMed: 11829602]
13. Chakrabartty A & Baldwin R Stability of α-Helices. 46, 141–176, doi:10.1016/s0065-3233(08)60334-4 (1995).
14. Bochicchio B, Pepe A & Tamburro AM Investigating by CD the molecular mechanism of elasticity of elastomeric proteins. Chirality 20, 985–994, doi:10.1002/chir.20541 (2008). [PubMed: 18293367]
15. Sreerama N & Woody RW Estimation of protein secondary structure from circular dichroism spectra: Comparison of CONTIN, SELCON, and CDSSTR methods with an expanded reference set. Anal. Biochem. 287, 252–260 (2000). [PubMed: 11112271]
16. Bernacki JP & Murphy RM Length-dependent aggregation of uninterrupted polyalanine peptides. Biochemistry 50, 9200–9211, doi:10.1021/bi201155g (2011). [PubMed: 21932820]

Author Manuscript

17. Muñoz V & Serrano L Elucidating the folding problem of helical peptides using empirical parameters. Nature Structural Biology 1, 399–409, doi:10.1038/nsb0694-399 (1994). [PubMed: 7664054]

18. Lacroix E, Viguera AR & Serrano L Elucidating the folding problem of alpha-helices: local motifs, long-range electrostatics, ionic-strength dependence and prediction of NMR parameters. J Mol Biol 284, 173–191, doi:10.1006/jmbi.1998.2145 (1998). [PubMed: 9811549]

19. Wright ER, McMillan RA, Cooper A, Apkarian RP & Conticello VP Thermoplastic elastomer hydrogels via self-assembly of an elastin-mimetic triblock polypeptide. Adv Funct Mater 12, 149–154, doi:Doi 10.1002/1616-3028(20020201)12:2<149::Aid-Adfm149>3.0.Co;2-N (2002).

20. Glassman MJ, Avery RK, Khademhosseini A & Olsen BD Toughening of Thermoresponsive Arrested Networks of Elastin-Like Polypeptides To Engineer Cytocompatible Tissue Scaffolds. Biomacromolecules 17, 415–426, doi:10.1021/acs.biomac.5b01210 (2016). [PubMed: 26789536]

21. Reguera J et al. Thermal Behavior and Kinetic Analysis of the Chain Unfolding and Refolding and of the Concomitant Nonpolar Solvation and Desolvation of Two Elastin-like Polymers. Macromolecules 36, 8470–8476, doi:10.1021/ma034572q (2003).

22. Cho Y et al. Hydrogen bonding of beta-turn structure is stabilized in D(2)O. J Am Chem Soc 131, 15188–15193, doi:10.1021/ja9040785 (2009). [PubMed: 19919159]

23. Ding F, Borreguero JM, Buldyrey SV, Stanley HE & Dokholyan NV Mechanism for the alpha-helix to beta-hairpin transition. Proteins 53, 220–228, doi:10.1002/prot.10468 (2003). [PubMed: 14517973]

24. Urry DW & Ji TH Distortions in circular dichroism patterns of particulate (or membranous) systems. Arch Biochem Biophys 128, 802–807 (1968). [PubMed: 5704309]

25. Urry DW, Starcher B & Partridge SM Coacervation of solubilized elastin effects a notable conformational change. Nature 222, 795–796 (1969). [PubMed: 5786200]

26. Muiznieks LD, Jensen SA & Weiss AS Structural changes and facilitated association of tropoelastin. Archives of Biochemistry and Biophysics 410, 317–323, doi:10.1016/s0003-9861(02)00719-1 (2003). [PubMed: 12573292]

27. Yeo GC, Keeley FW & Weiss AS Coacervation of tropoelastin. Adv Colloid Interface Sci 167, 94–103, doi:10.1016/j.cis.2010.10.003 (2011). [PubMed: 21081222]

28. Israelachvili JN, Mitchell DJ & Ninham BW Theory of self-assembly of hydrocarbon amphiphiles into micelles and bilayers. Journal of the Chemical Society, Faraday Transactions 2: Molecular and Chemical Physics 72, 1525–1568, doi:10.1039/F29767201525 (1976).

29. Dušek K Phase separation during the formation of three-dimensional polymers. Journal of Polymer Science Part B: Polymer Letters 3, 209–212, doi:10.1002/pol.1965.110030311 (1965).

30. Cirulis JT, Keeley FW & James DF Viscoelastic properties and gelation of an elastin-like polypeptide. Journal of Rheology 53, 1215, doi:10.1122/1.3177005 (2009).

31. Tamburro AM, De Stradis A & D'Alessio L Fractal aspects of elastin supramolecular organization. J Biomol Struct Dyn 12, 1161–1172, doi:10.1080/07391102.1995.10508805 (1995). [PubMed: 7669265]

32. Gustafsson MG Nonlinear structured-illumination microscopy: wide-field fluorescence imaging with theoretically unlimited resolution. Proc Natl Acad Sci U S A 102, 13081–13086, doi:10.1073/pnas.0406877102 (2005). [PubMed: 16141335]

33. Clarke AW et al. Tropoelastin massively associates during coacervation to form quantized protein spheres. Biochemistry 45, 9989–9996, doi:10.1021/bi0610092 (2006). [PubMed: 16906757]

34. Caiazzo M et al. Defined three-dimensional microenvironments boost induction of pluripotency. Nat Mater 15, 344–352, doi:10.1038/nmat4536 (2016). [PubMed: 26752655]

35. Engler AJ, Sen S, Sweeney HL & Discher DE Matrix elasticity directs stem cell lineage specification. Cell 126, 677–689, doi:10.1016/j.cell.2006.06.044 (2006). [PubMed: 16923388]

36. DiMarco RL & Heilshorn SC Multifunctional materials through modular protein engineering. Adv Mater 24, 3923–3940, doi:10.1002/adma.201200051 (2012). [PubMed: 22730248]

37. Fernandez-Colino A, Arias FJ, Alonso M & Rodriguez-Cabello JC Amphiphilic Elastin-Like Block Co-Recombinamers Containing Leucine Zippers: Cooperative Interplay between Both Domains Results in Injectable and Stable Hydrogels. Biomacromolecules 16, 3389–3398, doi:10.1021/acs.biomac.5b01103 (2015). [PubMed: 26391850]

Author Manuscript Author Manuscript Author Manuscript Author Manuscript

38. Xu C & Kopecek J Genetically engineered block copolymers: influence of the length and structure of the coiled-coil blocks on hydrogel self-assembly. Pharm Res 25, 674–682, doi:10.1007/s11095-007-9343-z (2008). [PubMed: 17713844]
39. Wright ER & Conticello VP Self-assembly of block copolymers derived from elastin-mimetic polypeptide sequences. 54, 1057–1073, doi:10.1016/S0169-409X(02)00059-5 (2002).
40. Martin L, Castro E, Ribeiro A, Alonso M & Rodriguez-Cabello JC Temperature-triggered self-assembly of elastin-like block co-recombinamers:the controlled formation of micelles and vesicles in an aqueous medium. Biomacromolecules 13, 293–298, doi:10.1021/bm201436y (2012). [PubMed: 22263638]
41. MacEwan SR et al. Phase Behavior and Self-Assembly of Perfectly Sequence-Defined and Monodisperse Multiblock Copolypeptides. Biomacromolecules 18, 599–609, doi:10.1021/acs.biomac.6b01759 (2017). [PubMed: 28094978]
42. Xia XX, Xu Q, Hu X, Qin G & Kaplan DL Tunable self-assembly of genetically engineered silk--elastin-like protein polymers. Biomacromolecules 12, 3844–3850, doi:10.1021/bm201165h (2011). [PubMed: 21955178]
43. Luo T & Kiick KL Noncovalent Modulation of the Inverse Temperature Transition and Self-Assembly of Elastin-b-Collagen-like Peptide Bioconjugates. J Am Chem Soc 137, 15362–15365, doi:10.1021/jacs.5b09941 (2015). [PubMed: 26633746]
44. Ray B, El Hasri S & Guenet JM Effect of polymer tacticity on the molecular structure of polyelectrolyte/surfactant stoichiometric complexes in solutions and gels. Eur Phys J E Soft Matter 11, 315–323, doi:10.1140/epje/i2003-10020-0 (2003). [PubMed: 15011034]
45. Ray B et al. Effect of Tacticity of Poly(N-isopropylacrylamide) on the Phase Separation Temperature of Its Aqueous Solutions. Polymer Journal 37, 234–237, doi:10.1295/polymj.37.234 (2005).
46. Amiram M, Luginbuhl KM, Li X, Feinglos MN & Chilkoti A Injectable protease-operated depots of glucagon-like peptide-1 provide extended and tunable glucose control. Proc Natl Acad Sci U S A 110, 2792–2797, doi:10.1073/pnas.1214518110 (2013). [PubMed: 23359691]
47. Nettles DL, Chilkoti A & Setton LA Applications of elastin-like polypeptides in tissue engineering. Adv Drug Deliv Rev 62, 1479–1485, doi:10.1016/j.addr.2010.04.002 (2010). [PubMed: 20385185]
48. Nettles DL et al. In situ crosslinking elastin-like polypeptide gels for application to articular cartilage repair in a goat osteochondral defect model. Tissue Eng Part A 14, 1133–1140, doi: 10.1089/tea.2007.0245 (2008). [PubMed: 18433311]
49. Ratner BD A pore way to heal and regenerate: 21st century thinking on biocompatibility. Regen Biomater 3, 107–110, doi:10.1093/rb/rbw006 (2016). [PubMed: 27047676]
50. Sussman EM, Halpin MC, Muster J, Moon RT & Ratner BD Porous implants modulate healing and induce shifts in local macrophage polarization in the foreign body reaction. Ann Biomed Eng 42, 1508–1516, doi:10.1007/s10439-013-0933-0 (2014). [PubMed: 24248559]

Reference Methods

51. Meyer DE & Chilkoti A Purification of recombinant proteins by fusion with thermally-responsive polypeptides. Nat Biotechnol 17, 1112–1115, doi:10.1038/15100 (1999). [PubMed: 10545920]
52. Schneider CA, Rasband WS & Eliceiri KW NIH Image to ImageJ: 25 years of image analysis. Nature Methods 9, 671–675, doi:10.1038/nmeth.2089 (2012). [PubMed: 22930834]
53. Karperien A FracLac for Image J, version 2.5 (http://rsb.info.nih.gov/ij/plugins/fraclac/FLHelp/Introduction.htm, 1999–2012).
54. Shao L, Kner P, Rego EH & Gustafsson MG Super-resolution 3D microscopy of live whole cells using structured illumination. Nat Methods 8, 1044–1046, doi:10.1038/nmeth.1734 (2011). [PubMed: 22002026]
55. Gustafsson MG et al. Three-dimensional resolution doubling in wide-field fluorescence microscopy by structured illumination. Biophys J 94, 4957–4970, doi:10.1529/biophysj.107.120345 (2008). [PubMed: 18326650]

Author Manuscript Author Manuscript Author Manuscript Author Manuscript

56. Wood WG, Wachter C & Scriba PC Experiences Using Chloramine-T and 1,3,4,6-Tetrachloro-3-Alpha,6-Alpha-Diphenylglycoluril (Iodogen) for Radioiodination of Materials for Radioimmunoassay. J Clin Chem Clin Bio 19, 1051–1056 (1981).

57. Diehl KH et al. A good practice guide to the administration of substances and removal of blood, including routes and volumes. J Appl Toxicol 21, 15–23 (2001). [PubMed: 11180276]

Author Manuscript
Author Manuscript
Author Manuscript
Author Manuscript

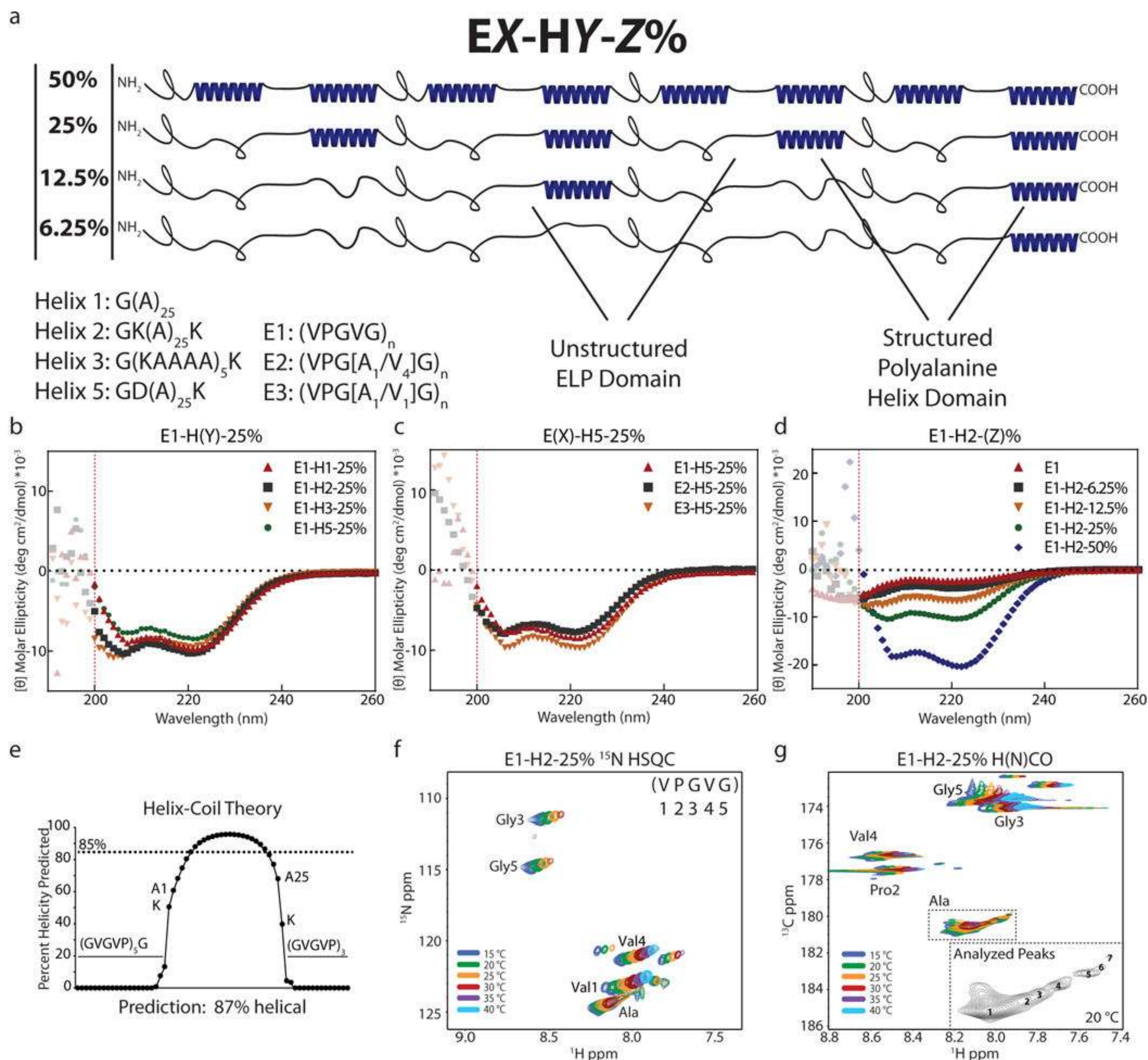

Figure 1: Partially ordered polymer library and structural characterization

(a) Recombinant POPs were constructed with 3 ELP components and 4 polyalanine helices at amino acid percentages up to 50%. UV-CD reveals definitive helical peaks at 222 and 208 nm, with peak amplitudes minimally altered by (b) polyalanine domain and (c) ELP but highly dependent on (d) total alanine content (dynode voltage >500 at <200nm; data not used for analysis). (e) This structural signature is consistent with helix-coil predictions (Agadir). (f) ^{15}N-HSQC and (g) H(N)CO (residue labels are the associated C' of the previous residue) 2D solution NMR spectra for E1-H2–25% were used to more precisely quantify total structural content. Each polyalanine domain was determined to have an average helicity of 90% (Supplementary Methods).

Author Manuscript

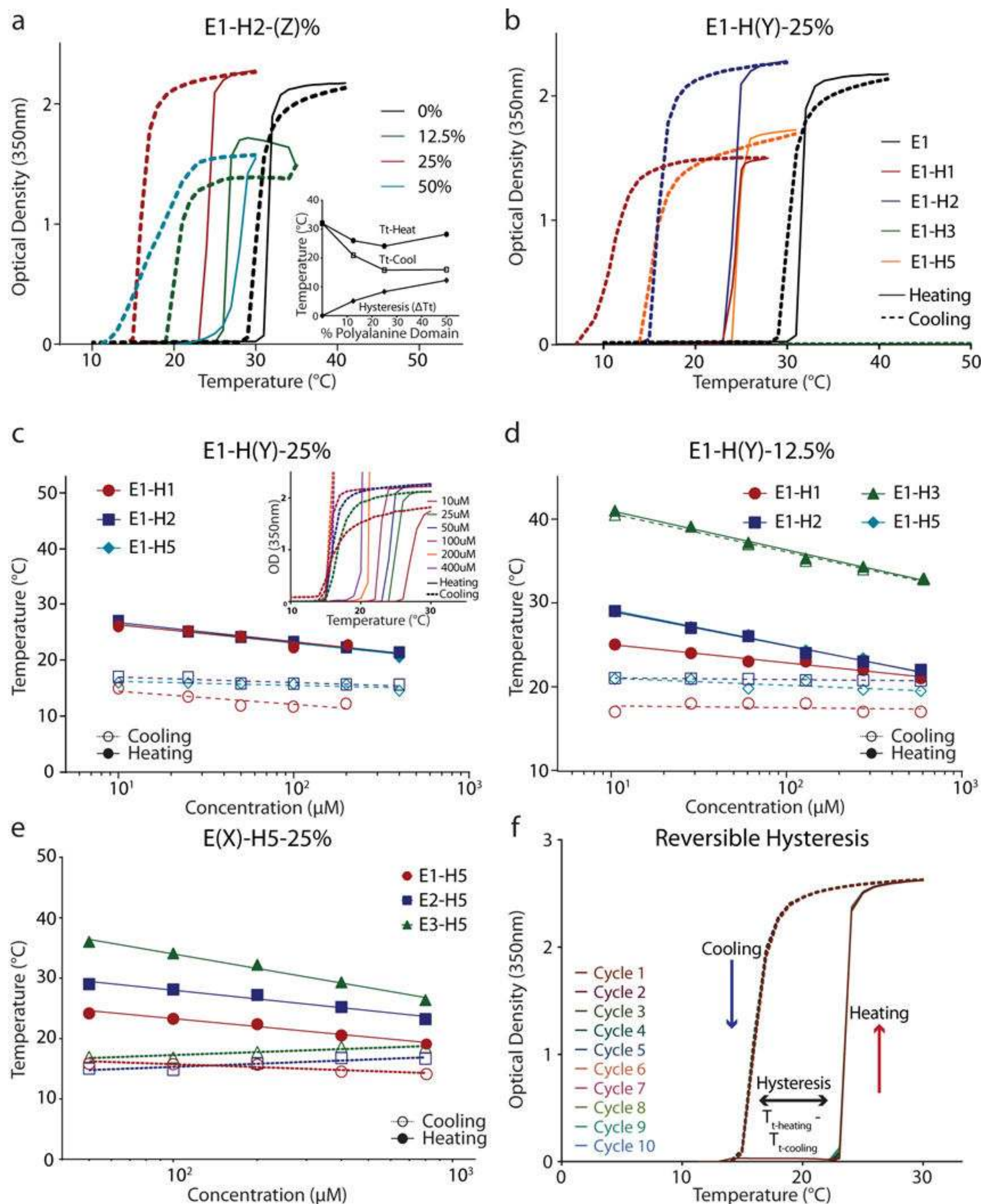

Figure 2: Phase behavior and tunable hysteresis

(a) OD measurements as a function of temperature show sharp, reversible phase behavior and hysteresis (ΔT_t). Hysteresis scales as a function of total helical content. (b-d) For a given E(X), the composition of the alanine domain modulates the T_t-heating and T_t-cooling with greater hydrophilicity leading to increased temperatures. Hysteresis is also dependent on the composition (charge distribution) of the polyalanine domains with an increase in charge producing a decrease in hysteresis. The T_t-cooling is concentration independent and solely determined by the polyalanine domains. (e) Therefore, for a given H(X), the T_t-heating can

Author Manuscript Author Manuscript Author Manuscript Author Manuscript

be independently controlled with ELP composition, providing a method to orthogonally control T_t-heating and T_t-cooling. (f) Polymers can be cyclically heated and cooled with no change in thermal behavior. Optical density measurements were taken at 350nm in PBS at 50μM unless otherwise indicated. Heating and cooling rates were kept at 1°C/min. OD amplitudes are non-interpretable due to difference in aggregate formation and settling.

Author Manuscript

Author Manuscript

Author Manuscript

Author Manuscript

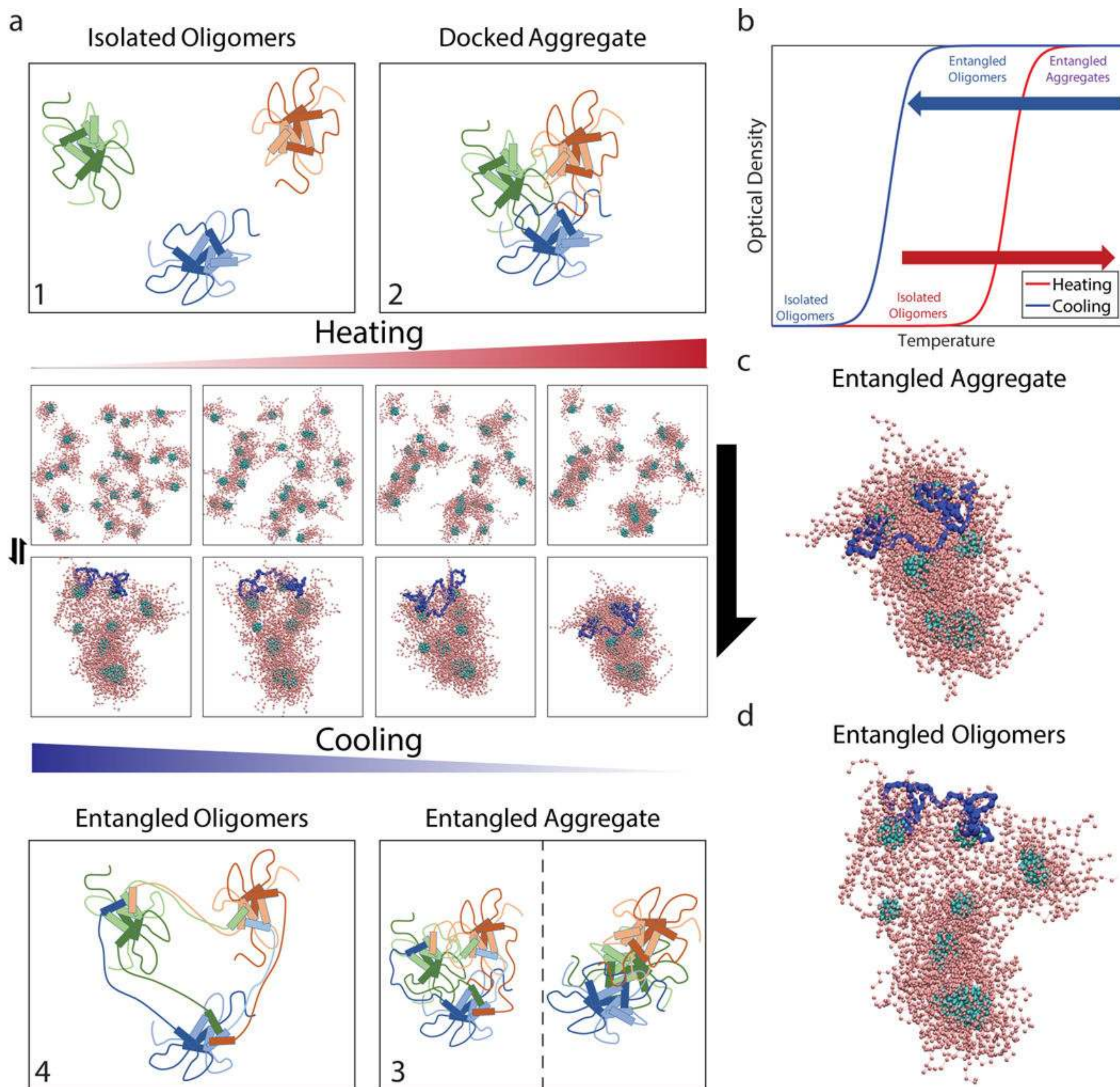

Figure 3: Proposed mechanism for hysteresis

(a) Simulations of the hysteretic cycle were performed using a coarse-grained bead-spring model for the POPs. Heating and cooling were achieved by modulating the interaction strengths between ELP domains. The interactions become favorable as temperature increases and the converse is true upon cooling. Snapshots extracted from phenomenological simulations of POPs are shown in the middle, surrounded by cartoon representations of the four states observed for POP during heating and cooling. Rod-like objects represent polyalanine domains and string-like tethers represent ELPs. The colors indicate their initial cluster with shading indicating different proteins in the same initial cluster. The one-sided

Author Manuscript Author Manuscript Author Manuscript Author Manuscript

arrows provide a pictorial summary of the expected rates for transitions between different states (fast for 2–3 and slow for 4–1). Within entangled aggregates we observe two types of morphologies *viz.*, entangled spheres or entangled cylinders. There is a reversible spheres to cylinders transition at even higher temperatures. (b) A sketch of the experimental observable as a function of heating / cooling *viz.*, the optical density is annotated by the species populating each regime. (c-d) Enlarged snapshots from the cooling arm of panel (a) demonstrate that the highlighted POP is not able to isolate itself into a single cluster and that the decrease in aggregate density is limited by the presence of domain swapped proteins.

Author Manuscript Author Manuscript Author Manuscript Author Manuscript

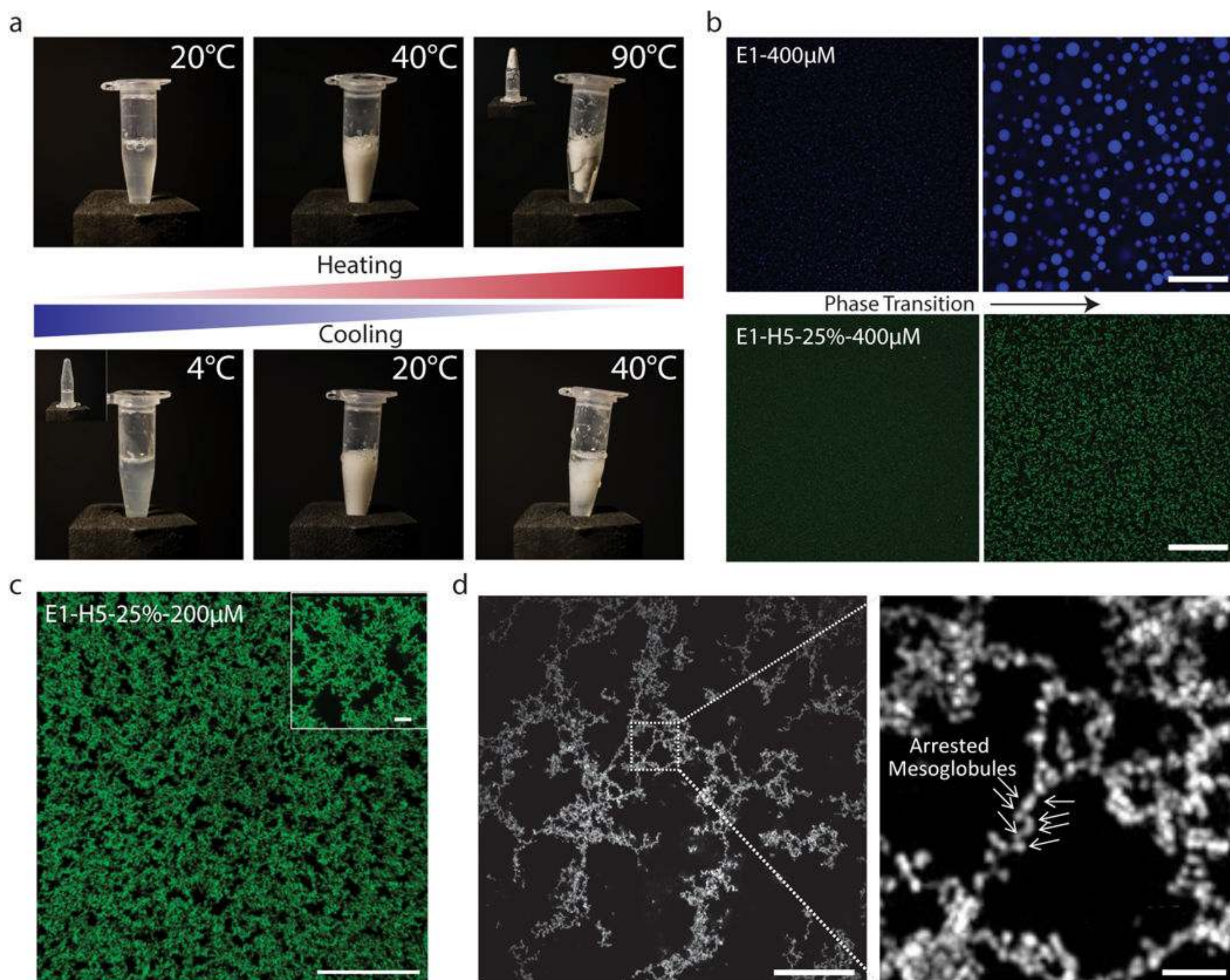

Figure 4: Arrested phase separation into fractal networks

(a) E1-H5–25% (2 mM, PBS) aggregation during a heating and cooling cycle shows a reversible transition from an optically translucent liquid to an opaque solid-like structure (passes inversion test) with syneresis observed at higher temperatures. (b) At the microscale, E1 and E1-H5–25% (400 μM, PBS) form liquid-like coacervates and fractal networks, respectively; scale bar 50 μm and 10μM for insert. (c) The intricacy of the network is more clearly seen with a 20 μm thick 3D reconstruction of E1-H5–25% (200 μM, PBS); scale bar 50 μM and 10 μM for the insert. (d) Network architecture at the meso scale is that of interconnected beads, as revealed by SIM; scale bars 10 μm (left) and 1 μm (right).

Author Manuscript Author Manuscript Author Manuscript Author Manuscript

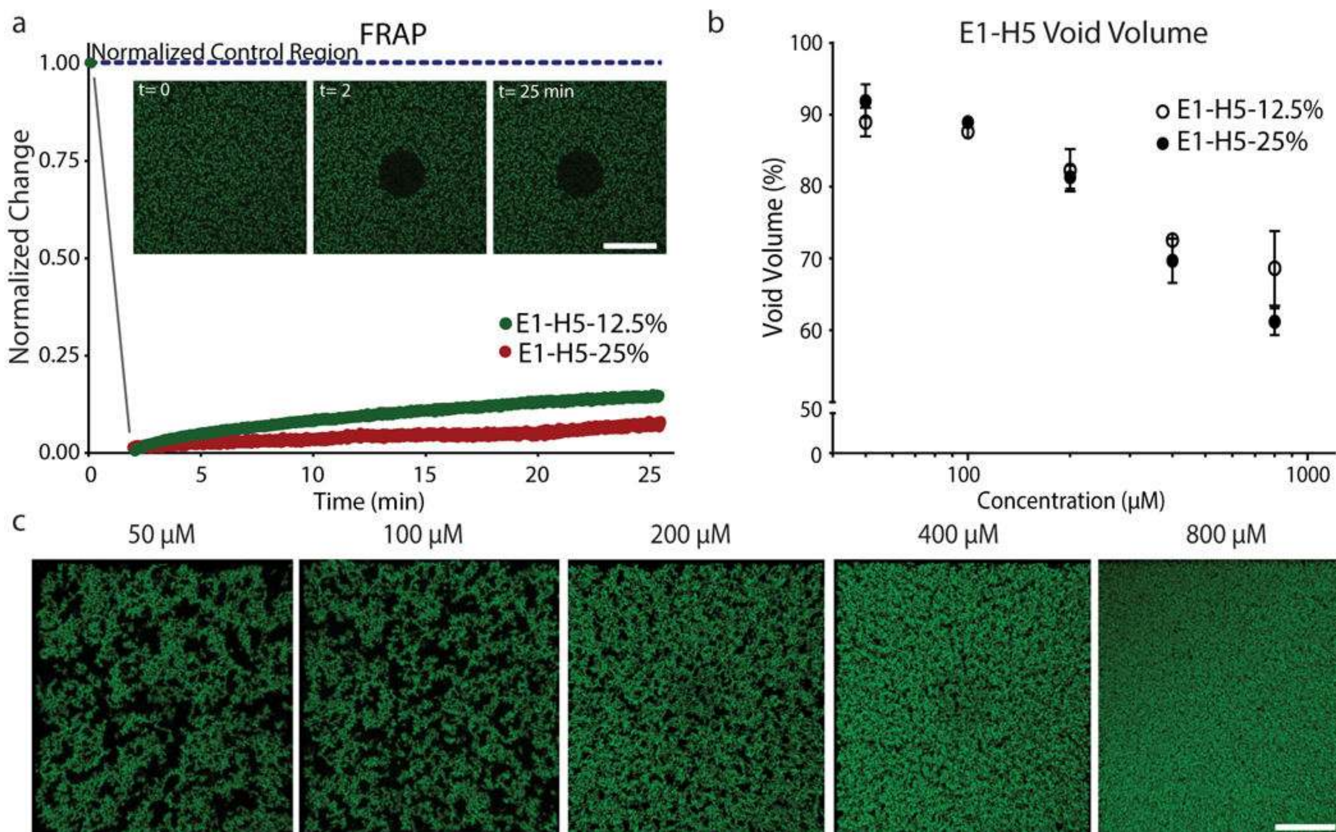

Figure 5: Network stability and void volume

(a) As determined by the limited fluorescence recovery 25 min after bleaching, 12.5% and 25% networks have a high kinetic stability and limited liquid-like properties; Inset pictures are shown for E1-H5–25% at 400 μM. (b-c) Void volumes can be tuned from 60–90% by altering polymer concentration. Data represent mean ± SEM (n=4 independent samples). Scale bars are 50 μm.

Author Manuscript

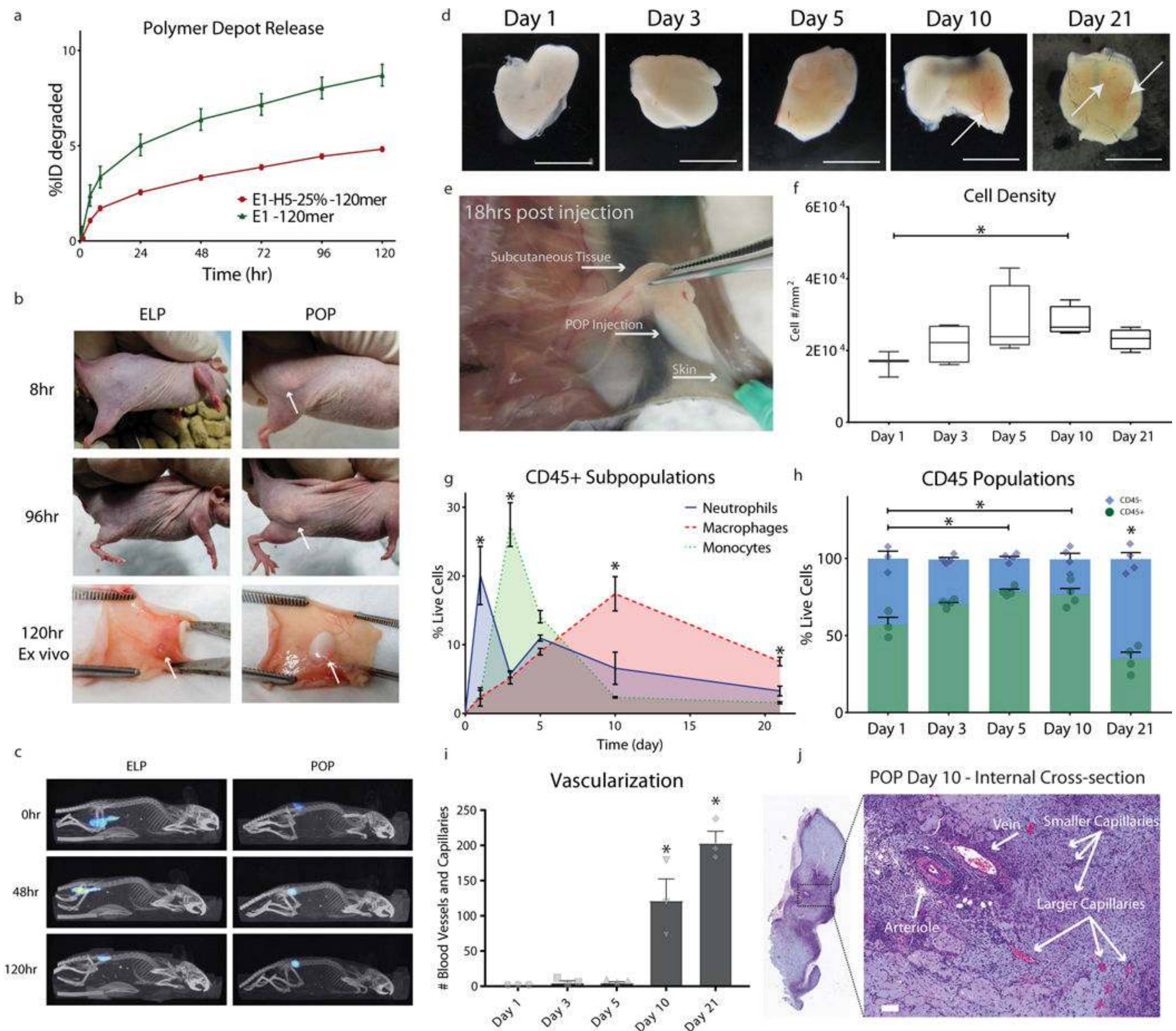

Figure 6: In vivo stability and tissue incorporation of POPs

(a) E1-H5–25% POP s.c. injections were significantly more stable than their E1 counterparts with just 5% of the injected dose degraded at 120hrs; 200μl 250μM injections; $p<0.05$ for all data points after 0hr, determined by two-tailed t-tests (n=6 mice); data represent mean ± SEM. (b) Whereas ELPs diffuse into the s.c. space, POP depots were externally apparent, retaining the shape and volume of the initial injection up to dissection and ex vivo analysis. (c) Representative CT-SPECT images of the depots confirm increased diffusivity of ELPs and increased stability of POPs. (d) POPs were injected into BL/6 mice and explanted for analysis over 21 days. Representative images are shown with arrows pointing at externally evident vascularization. Scale bars 5mm. (e) POPs rapidly integrated into the subcutaneous environment with sufficient strength to endure moderate extension less than 24 hours after injection. (f) There is a high initial cell incorporation with some change over the observed time periods; for *, $p<0.05$ determined by ANOVA with Tukey post-hoc (D1 n=3, D3–21

Author Manuscript Author Manuscript Author Manuscript Author Manuscript

n=4); data presented as 10–90% box plots. (g) Flow cytometry for cells involved in the innate immune reveals subsequent spikes in neutrophils, inflammatory monocytes, and macrophages, with a loss in all hematopoietic cells (CD45+) by day 21; for *, $p<0.05$ determined by ANOVA with Tukey post-hoc (D1 n=3, D3–21 n=4); data represent mean ± SEM. (i) The loss in inflammation corresponds with an increase in vascularization, quantified by number of visible capillaries in histological sections; for *, $p<0.05$ as determined by ANOVA with Tukey post-hoc (n=3); data represent mean ± SEM. (j) An example tissue slice 10 days post injection shows an area of particularly high vascularization density (scale bar 100μm). Additional images given in the supplementary information.